Delaying dynamic wetting failure using thermal Marangoni flow

Ninad V. Mhatre [1], Marcio S. Carvalho [2], and Satish Kumar [1,*]
[1]Department of Chemical Engineering and Materials Science, University of Minnesota, Minneapolis, Minnesota 55455, USA
[2]Department of Mechanical Engineering, Pontificia Universidade Catòlica do Rio de Janeiro, Rio de Janeiro, RJ, 22451-041, Brazil

(Received 15 June 2022; accepted 15 November 2022; published 19 December 2022)

Coating processes are limited by the onset of dynamic wetting failure beyond a critical substrate speed. In this work, we study the influence of thermal Marangoni flow on dynamic wetting with the objective of delaying wetting failure to higher substrate speeds. A two-dimensional hydrodynamic model is developed to examine steady-state dynamic wetting of a Newtonian liquid in a parallel-plate geometry where a temperature gradient between the plates generates thermal Marangoni flow. The dynamics of the air displaced by the liquid are accounted for, and the Galerkin finite-element method is used to calculate steady-state solutions and find the critical substrate (bottom plate) speed at which wetting failure occurs. It is found that thermal Marangoni flow directed toward the dynamic contact line at the substrate delays wetting failure to a higher speed, whereas flow away from the contact line causes wetting failure at a lower speed. Flow toward the contact line reduces the bending of the air-liquid interface and increases the thickness of the air film near the contact line. This lowers the magnitude of pressure gradients in the air phase and facilitates removal of air from the contact line, delaying the entrainment of air and consequently wetting failure to higher speeds. In contrast, flow away from the contact line increases interface bending at a given speed, leading to thinning of the air film near the contact line and causing wetting failure at lower speeds. The findings presented in this study suggest a novel strategy for designing faster coating processes through the application of thermal Marangoni flow.

DOI: 10.1103/PhysRevFluids.7.124002

I. INTRODUCTION

Dynamic wetting involves the displacement of one fluid by another on a solid substrate. The displaced fluid is called the receding phase and the displacing fluid is called the advancing phase. This phenomenon is important in areas as diverse as microfluidics and oil recovery [1–3]. Dynamic wetting also plays a key role in coating processes, where the coating liquid (advancing phase) displaces the air (receding phase) which surrounds the surface to be coated [4]. Increasing the substrate speed beyond a critical value (denoted by U_{crit}) leads to incomplete displacement of the air, causing dynamic wetting failure. The onset of wetting failure is accompanied by a transition from steady two-dimensional flow to a transient three-dimensional flow and the entrainment of air in the liquid phase [5]. This leads to nonuniformity in the coating layer and worsens product quality [6,7]. As a result, coating processes are operated below U_{crit} to ensure steady dynamic wetting, but this limits the production rate. Thus, delaying the onset of wetting failure to a higher U_{crit} enables faster coating processes. In this work, we use numerical simulations to investigate the influence of thermal

*kumar030@umn.edu

Marangoni flow on dynamic wetting failure in a model geometry, with the objective of delaying wetting failure to higher speeds.

Marangoni flow is generated due to the presence of surface-tension gradients at a fluid-fluid interface and is directed from low-surface-tension regions to high-surface-tension regions [8]. Surface-tension gradients can be caused by solute concentration gradients or temperature gradients at a fluid-fluid interface, and the resultant flows are called solutal Marangoni flow and thermal Marangoni flow, respectively [9]. It should be noted that all the examples of solutal Marangoni flow discussed in this work refer to systems where the solute is a surfactant. Generally, the surface tension at a fluid-fluid interface decreases with increasing surfactant concentration and temperature. As a result, in the presence of surfactant concentration or temperature gradients, the resultant Marangoni flow is driven from high-surfactant-concentration to low-surfactant-concentration regions (solutal Marangoni flow) or from high-temperature to low-temperature regions (thermal Marangoni flow) [10].

Liu *et al.* conducted a theoretical study to examine the effects of solutal Marangoni flow on dynamic wetting failure in a parallel-plate geometry, where the bottom plate moves to the right with a fixed speed and the top plate is stationary [11]. A Newtonian liquid and air along with insoluble surfactant are confined between the two plates. When the liquid (advancing phase) displaces the air (receding phase) completely, steady dynamic wetting occurs. It was found that the presence of surfactant caused wetting failure to occur at a lower capillary number (dimensionless number proportional to substrate speed) compared to a system where surfactant is absent. This occurs because of the accumulation of surfactant near the bottom plate due to the flow in the liquid, generating a solutal Marangoni flow away from the contact line at the bottom plate. The predicted decrease in the critical substrate speed is qualitatively consistent with experimental observations [11,12].

In the absence of Marangoni flow, dynamic wetting failure occurs when the capillary-stress gradients (arising due to the curvature gradients at the air-liquid interface) cannot support the pressure gradients required to push the air away from the contact line at the bottom plate [13]. The solutal Marangoni flow generated due to the presence of insoluble surfactant causes thinning of the air film near the contact line, which increases the magnitude of the pressure gradients in the air, leading to wetting failure at a lower capillary number [11,14,15]. In the presence of soluble surfactants, desorption of surfactant from the air-liquid interface to the bulk liquid decreases the surfactant concentration gradient at the interface, which decreases the magnitude of the Marangoni stresses and thickens the air film near the contact line (compared to the case of insoluble surfactants). As a consequence, wetting failure occurs at a higher capillary number [12].

Since Marangoni flow directed away from the dynamic contact line causes wetting failure at a lower capillary number, we hypothesize that wetting failure can be delayed to a higher capillary number by reversing the direction of Marangoni flow. The direction of solutal Marangoni flow in the parallel-plate geometry is controlled by the flow in the liquid phase and cannot readily be reversed [11]. In this work, we introduce a temperature gradient between the two plates, which generates a thermal Marangoni flow in the system, the direction of which can controlled by altering the temperature gradient. A higher temperature at the top plate generates a thermal Marangoni flow directed toward the dynamic contact line at the bottom plate, and a higher temperature at the bottom plate drives thermal Marangoni flow away from that contact line. We show via finite-element calculations that the direction of thermal Marangoni flow in the parallel-plate geometry affects the onset of wetting failure, with thermal Marangoni flow directed toward the contact line delaying wetting failure to a higher capillary number. The findings reported in this work suggest a novel strategy for designing faster coating processes through the application of thermal Marangoni flow.

The model formulation is discussed in Sec. II, the effects of thermal Marangoni flow on important characteristics such as the critical speed and the shape of the air-liquid interface are presented in Sec. III, the influence of thermal Marangoni flow on the wetting-failure mechanism is discussed in Sec. IV, and a summary of our findings is given in Sec. V.

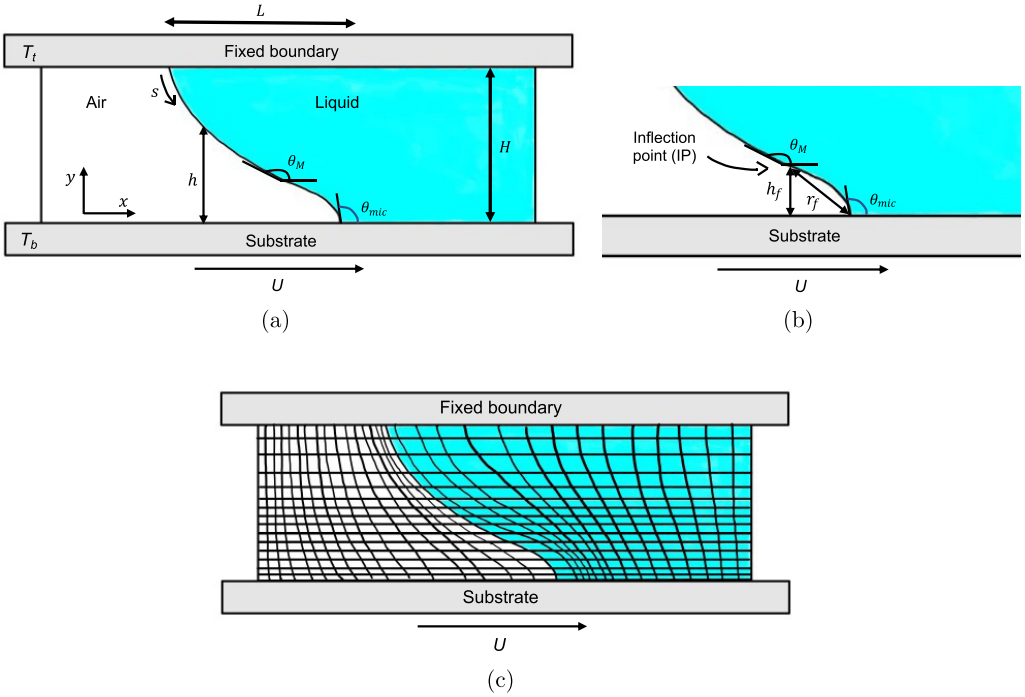

FIG. 1. (a) Schematic of the model geometry. (b) Enlarged view of the interface near the inflection point showing θ_M, θ_{mic}, and the location of the inflection point with respect to the substrate. (c) Schematic of the finite-element mesh used for discretizing the model equations.

II. MODEL FORMULATION

A hydrodynamic model is developed to study the displacement of air by a Newtonian liquid in a parallel-plate geometry in the presence of thermal Marangoni flow [Fig. 1(a)]. The bottom plate (substrate) moves to the right with a speed U and is located at a distance H from the top plate, which serves as a fixed upper boundary. The intersection of the solid, liquid, and air phases is called the contact line, and our model system has two contact lines: one at the moving bottom substrate and another at the fixed upper boundary.

Figure 1(a) shows two contact angles near the moving substrate: the microscopic contact angle (θ_{mic}), which is the angle between the air-liquid interface and the moving substrate at the contact line, and the apparent contact angle (θ_M), which is the angle measured at some distance from the contact line. In this work, θ_M is taken to be the maximum angle along the air-liquid interface, and it is found at an inflection point (IP). θ_M is a measure of the interface deformation, with a larger θ_M value indicating a larger extent of interface deformation. The interface height is denoted by h and the horizontal length of the interface is denoted by L.

Figure 1(b) shows an enlarged view of the interface near the IP. The height of the IP is denoted by h_f and the distance between the contact line and the IP is denoted by r_f. A temperature gradient is introduced between the fixed upper boundary and the substrate to generate thermal Marangoni flow in the system. The temperatures of the fixed boundary (top plate) and the moving substrate (bottom plate) are denoted by T_t and T_b, respectively.

A. Governing equations and boundary conditions

Inertial effects are neglected in this work, giving rise to the creeping-flow equations, which along with the energy balance equation constitute the governing equations for the model:

$$\nabla \cdot \mathbf{v} = 0, \quad \nabla p = \nabla^2 \mathbf{v}, \tag{2.1}$$

$$\mathrm{Pe}\,(\mathbf{v} \cdot \nabla T) = \nabla^2 T, \tag{2.2}$$

where $\mathbf{v}$, p, and T represent the fluid velocity, pressure, and temperature in a given phase, respectively. The characteristic scales used for lengths, velocities, and stresses are H, U, and $\mu U/H$, respectively, where μ is the viscosity (assumed to be constant) of the respective phase, and the temperature is nondimensionalized as $(T - T_b)/(T_t - T_b)$. Pe is the thermal Peclet number, which is the ratio of the rates of convective energy transfer to diffusive energy transfer and is defined as UH/α for each phase, where α is the thermal diffusivity of the respective phase. We use a linear equation of state that incorporates the dependence of surface tension (σ) on temperature for simplicity, and because it exhibits a good agreement with experimental findings [16–18],

$$\sigma = \sigma_b - k_t(T - T_b), \tag{2.3}$$

where σ_b is the surface tension corresponding to T_b and k_t is the rate of change of the surface tension with temperature. The variation of viscosity with temperature in both the phases has been neglected to isolate the effects of thermal Marangoni flow. Similarly, we neglect gravitational effects, which corresponds to assuming that the Bond number ($\mathrm{Bo} = \rho g H^2/\sigma$, ratio of gravitational to surface-tension forces) and the Stokes number ($\mathrm{St} = \rho g H^2/\mu U$, ratio of gravitational to viscous forces) are small.

The hydrodynamic model is completed by imposing the following dimensionless boundary conditions at the air-liquid interface:

$$\mathbf{v}|_{\mathrm{air}} = \mathbf{v}|_{\mathrm{liq}}, \tag{2.4}$$

$$\mathbf{n} \cdot \mathbf{v} = 0, \tag{2.5}$$

$$M_t \nabla_s \sigma \cdot t = \mathbf{n} \cdot \mathbf{T} \cdot \mathbf{t}|_{\mathrm{liq}} - \mathbf{n} \cdot \mathbf{T} \cdot \mathbf{t}|_{\mathrm{air}}, \tag{2.6}$$

$$\kappa(1/\mathrm{Ca} + \sigma M_t) = \mathbf{n} \cdot \mathbf{T} \cdot \mathbf{n}|_{\mathrm{liq}} - \mathbf{n} \cdot \mathbf{T} \cdot \mathbf{n}|_{\mathrm{air}}, \tag{2.7}$$

$$T|_{\mathrm{air}} = T|_{\mathrm{liq}}, \tag{2.8}$$

$$\mathbf{n} \cdot \nabla T|_{\mathrm{air}} = k_r \mathbf{n} \cdot \nabla T|_{\mathrm{liq}}, \tag{2.9}$$

where (2.4) is the velocity continuity condition; (2.5) is the kinematic condition; (2.6) and (2.7) are the tangential stress balance and normal stress balance, respectively; (2.8) is the temperature continuity condition; and (2.9) is the energy flux balance. Here ∇_s is the surface gradient operator; κ is the interface curvature; $\mathbf{n}$ and $\mathbf{t}$ are the normal and tangent unit vectors at the interface, respectively; and $\mathbf{T}$ is the Newtonian stress tensor. The stress tensor for the air phase contains the viscosity ratio ($\chi = \mu_{\mathrm{air}}/\mu_{\mathrm{liq}}$) and has the form $\mathbf{T} = -p\mathbf{I} + \chi[\nabla \mathbf{v} + \nabla \mathbf{v}^T]$, where $\mathbf{I}$ is the identity tensor.

Surface tension is nondimensionalized as $(\sigma - \sigma_t)/(\sigma_b - \sigma_t)$, where σ_t and σ_b are the surface tensions corresponding to T_t and T_b, respectively. The following dimensionless parameters arise: the viscosity ratio ($\chi = \mu_{\mathrm{air}}/\mu_{\mathrm{liq}}$) which is the ratio of air viscosity to liquid viscosity; the capillary number ($\mathrm{Ca} = \mu_{\mathrm{liq}} U/\sigma_t$), which is the ratio of viscous forces to capillary forces; the thermal Marangoni number [$M_t = k_t(T_t - T_b)/(\mu_{\mathrm{liq}} U)$], which is the ratio of surface-tension forces to viscous forces; and the thermal conductivity ratio ($k_r = k_{\mathrm{liq}}/k_{\mathrm{air}}$), which is the ratio of liquid thermal conductivity to air thermal conductivity. The capillary number at the critical substrate speed (U_{crit}) is defined as the critical capillary number ($\mathrm{Ca}_{\mathrm{crit}} = \mu_{\mathrm{liq}} U_{\mathrm{crit}}/\sigma_t$) and it indicates the onset of dynamic wetting failure. A discussion of these dimensionless parameters is presented in Sec. II C.

The contact line at the fixed upper boundary is pinned, while the contact line at the substrate (bottom plate) is allowed to slip along the moving substrate. This approach is consistent with prior studies and is motivated by the slot-die coating process where the top contact line at the upstream meniscus is pinned to the slot-die head, and the bottom contact line can move on the solid to be coated [11,13,19]. Due to the motion of the contact line at the substrate, applying the no-slip

condition causes a stress singularity. This is remedied by using a Navier slip condition [20,21]:

$$\mathbf{t_s} \cdot (\mathbf{v} - \mathbf{U})|_{y=0} = \lambda[\mathbf{n_s} \cdot \mathbf{T} \cdot \mathbf{t_s}]|_{y=0}, \tag{2.10}$$

where $\lambda = l_s/H$ is the dimensionless slip length and l_s is the dimensional slip length. $\mathbf{U}$ is the velocity vector of the substrate (which has only a horizontal component in this work), $\mathbf{n_s}$ is the unit normal vector to the substrate, and $\mathbf{t_s}$ is the unit tangent vector to the substrate.

Temperature continuity is applied along the moving substrate for both the phases,

$$T|_{y=0} = 0. \tag{2.11}$$

At the fixed upper boundary, the no-slip, no-penetration, and temperature continuity conditions are applied for both phases:

$$\mathbf{v}|_{y=1} = 0, \tag{2.12}$$

$$T|_{y=1} = 1, \tag{2.13}$$

Prior theoretical studies have reported good agreement between numerical results and experimental findings by using a fixed value of θ_{mic} and we use a similar approach in this work by fixing $\theta_{\text{mic}} = 90^\circ$ (further discussion is presented in Sec. II C) [11,22,23]. We assume that the flow is fully developed, and the normal heat flux is zero, at the left and right boundaries [Fig. 1(a)]. The governing equations (2.1)–(2.2) along with the boundary conditions (2.3)–(2.13) constitute the hydrodynamic model.

B. Solution method

The hydrodynamic model described in Sec. II A is discretized using the Galerkin finite-element method and the resulting system of nonlinear equations is solved using the Newton-Raphson method. This is done using Goma 6.0, which is a multiphysics finite-element tool that employs a pseudosolid domain mapping method for describing mesh motion [24]. Biquadratic basis functions are used to discretize velocity, temperature, and mesh coordinates (x and y values), and linear discontinuous basis functions are used to discretize the pressure. The basis functions are chosen based on prior work [11,13,22,23].

Figure 1(c) shows a schematic of the finite-element mesh. The meshes used in this work are generated using Coreform Cubit 2020.2 [25]. We concentrated the elements near the contact lines to accurately capture the interface bending at high substrate speeds. The mesh is refined until the results are mesh independent (a variation of less than 0.2% in the results on further refinement), and a final mesh consisting of 12 000 elements is found to be sufficient; this mesh is used for all the calculations. The model is validated against prior theoretical studies where thermal Marangoni flow was absent [5,13].

C. Dimensionless parameters

We consider an air-water system (air is the receding phase and water is the advancing phase) for our simulations and the values of physical properties are chosen accordingly [26]. A temperature difference of 5°C between the plates is used for our calculations. Table I lists the order of magnitude of all the dimensionless parameters discussed in Sec. II A. The influence of the dimensionless slip length on wetting failure has been studied in prior work, and Ca_{crit} is found to increase with increasing λ, but the qualitative features of the results do not vary with λ [13,22]. We report all the results in this work for a single λ to isolate the effects of thermal Marangoni flow, and based on calculations at different values of λ, $\lambda = 10^{-2}$ (e.g., $l_s = 10^{-7}$ m and $H = 10^{-5}$ m) is chosen for computational ease. Some additional calculations for different values of λ are shown in Appendix A 1.

TABLE I. Dimensionless parameters and their order of magnitude.

Dimensionless parameter	Definition	Magnitude
Viscosity ratio	$\chi = \mu_{air}/\mu_{liq}$	0.0179
Dimensionless slip length	$\lambda = l_s/H$	10^{-2}
Thermal conductivity ratio	$k_r = k_{liq}/k_{air}$	29.8
Microscopic contact angle	θ_{mic}	90°
Liquid Peclet number	$Pe_{liq} = UH/\alpha_{liq}$	0–10^2
Air Peclet number	$Pe_{air} = UH/\alpha_{air}$	0–10^0
Thermal Marangoni number	$M_t = k_t(T_t - T_b)/(\mu_{liq}U)$	10^0–10^4
Capillary number	$Ca = \mu_{liq}U/\sigma_t$	0–4.56

Generally, the microscopic contact angle may depend on parameters such as the substrate speed, liquid viscosity, and surface tension [27–29]. However, the model can be simplified by assuming that θ_{mic} remains constant, and using this approach gives reasonably good agreement with experimental findings [22,30]. It is found that Ca_{crit} increases with decreasing θ_{mic}, but the qualitative features of the results do not vary with θ_{mic} [13,22]. As a consequence, we report all the results in this work for a single microscopic contact angle ($\theta_{mic} = 90^\circ$) to isolate the effects of thermal Marangoni flow.

In our simulations, the speed of the substrate is increased until the critical substrate speed is reached (this process is explained in Sec. III). The physical properties of both phases do not change with substrate speed. As a consequence, the magnitudes of the substrate-speed-dependent dimensionless parameters (Pe_{liq}, Pe_{air}, M_t, and Ca) vary as the substrate speed increases. Table I shows the range of magnitudes for these dimensionless groups.

It should be noted that $M_t > 0$ when $T_t > T_b$, and thermal Marangoni flow is directed toward the contact line at the bottom plate [Fig. 1(a)]. Similarly, $M_t < 0$ when $T_t < T_b$, and thermal Marangoni flow is directed away from the contact line at the bottom plate.

III. INFLUENCE OF THERMAL MARANGONI FLOW ON WETTING FAILURE

In this work, we study three cases: (i) thermal Marangoni flow toward the contact line at the bottom plate ($M_t > 0$), (ii) thermal Marangoni flow away from the contact line at the bottom plate ($M_t < 0$), and (iii) absence of thermal Marangoni flow ($M_t = 0$). For each case, the value of Ca_{crit} is calculated by tracing a steady-state solution family which tracks the evolution of θ_M as Ca increases (indicating an increase in substrate speed). Figure 2 illustrates typical solution families and interface profiles for all the cases. In this section, we discuss the influence of thermal Marangoni flow on the critical capillary number and the interface shape.

A. Solution families

Figure 2(a) shows the solution families, and for all the cases, θ_M increases with Ca until a turning point is reached. Since the magnitude of θ_M is a measure of interface bending [Fig. 1(a)], the solution families indicate that increasing the substrate speed causes more interface deformation. Beyond the turning point, two-dimensional (2D) steady-state solutions cannot be obtained, which suggests a transition from steady dynamic wetting to a transient 3D flow, indicating the onset of wetting failure (as discussed in Sec. I) [13,31]. As a consequence, the capillary number at the turning point represents a critical capillary number (Ca_{crit}). The turning point separates the stable (lower) branch from the unstable (upper) branch of the solution family, along which θ_M increases as Ca decreases [32,33]. Goma has in-built arclength continuation capabilities which have been used to obtain solutions along the unstable branch. We could recover only a small portion of the unstable branch due to limitations associated with mesh distortion, but it is sufficient to identify the turning point.

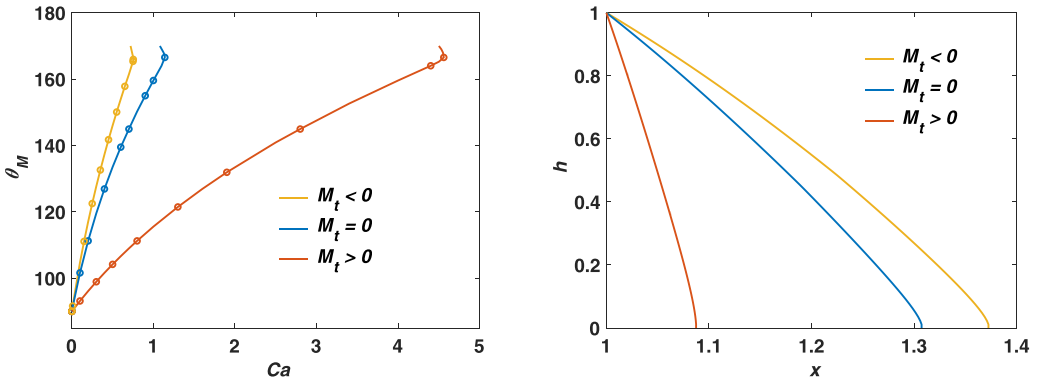

FIG. 2. (a) Solution families for (i) $M_t > 0$ ($1.28 < M_t < 9893.4$), which corresponds to flow toward contact line ($\mathrm{Ca_{crit}} = 4.56$); (ii) $M_t < 0$ ($-9821.7 < M_t < -5.76$), which corresponds to flow away from contact line ($\mathrm{Ca_{crit}} = 0.753$); and (iii) $M_t = 0$, which corresponds to the absence of thermal Marangoni flow ($\mathrm{Ca_{crit}} = 1.14$). (b) Interface profiles for all the cases at $\mathrm{Ca} = 0.2$.

Figure 2(a) shows that the largest $\mathrm{Ca_{crit}}$ is obtained for $M_t > 0$, followed by $M_t = 0$ and $M_t < 0$. This indicates that thermal Marangoni flow toward the contact line at the bottom plate ($M_t > 0$) delays wetting failure to a higher $\mathrm{Ca_{crit}}$, whereas thermal Marangoni flow away from the contact line ($M_t < 0$) causes wetting failure at a lower $\mathrm{Ca_{crit}}$. This result is consistent with the findings of Liu *et al.*, where Marangoni flow directed away from the contact line causes wetting failure at a lower $\mathrm{Ca_{crit}}$ [11]. It should also be noted that the solution family reaches $\mathrm{Ca_{crit}}$ at approximately the same apparent contact angle ($\theta_M \approx 168^\circ$) for all the cases, which suggests that the interface shape near the contact line is similar when the system is nearing the transition to wetting failure. The influence of thermal Marangoni flow on the interface shape is discussed in Sec. III B.

For the parameter values used in Fig. 2, thermocapillarity can produce significant changes in the critical substrate speed for moderate temperature differences. For example, making the top plate 10°C hotter would increase the critical substrate speed by ∼80% relative to the case of no Marangoni flow. Similarly, making the bottom plate 10°C hotter would reduce the critical substrate speed by ∼60%.

We have checked whether all solution families in Fig. 2(a) can collapse onto a single curve by redefining an effective capillary number $\mathrm{Ca_{eff}} = \mu_{\mathrm{liq}} U/\sigma_{\mathrm{eff}}$, where σ_{eff} is the effective surface tension that occurs at a corresponding dimensionless temperature T_{eff}. We determine the σ_{eff} for both the cases with nonzero M_t such that the respective solution families collapse onto the curve for $M_t = 0$. For $M_t > 0$, $\sigma_{\mathrm{eff}} = 3.91\sigma_{\mathrm{water}}$ and $T_{\mathrm{eff}} = 1.8$, and for $M_t < 0$, $\sigma_{\mathrm{eff}} = 0.68\sigma_{\mathrm{water}}$ and $T_{\mathrm{eff}} = -0.48$. The T_{eff} values lie outside the dimensionless temperature range defined in the model geometry (0 to 1) and a discrepancy is observed in the rescaled solution families near the turning point. As a consequence, we conclude that the solution families cannot be rescaled in a physically reasonable manner such that they collapse onto a single curve.

Finally, while the calculations in Fig. 2 are for a given applied temperature difference between the plates (5°C), additional calculations for different temperature differences (and thus different ranges of thermal Marangoni numbers) are given in Appendix A 2. Changes to the applied temperature difference change the values of the capillary numbers but not the qualitative behavior of the solution families.

B. Interface shapes and temperature contours

Figure 2(b) shows the interface shapes for all the cases at a fixed capillary number ($\mathrm{Ca} = 0.2$). The contact line at the top plate is pinned for all the cases while the contact line at the bottom plate

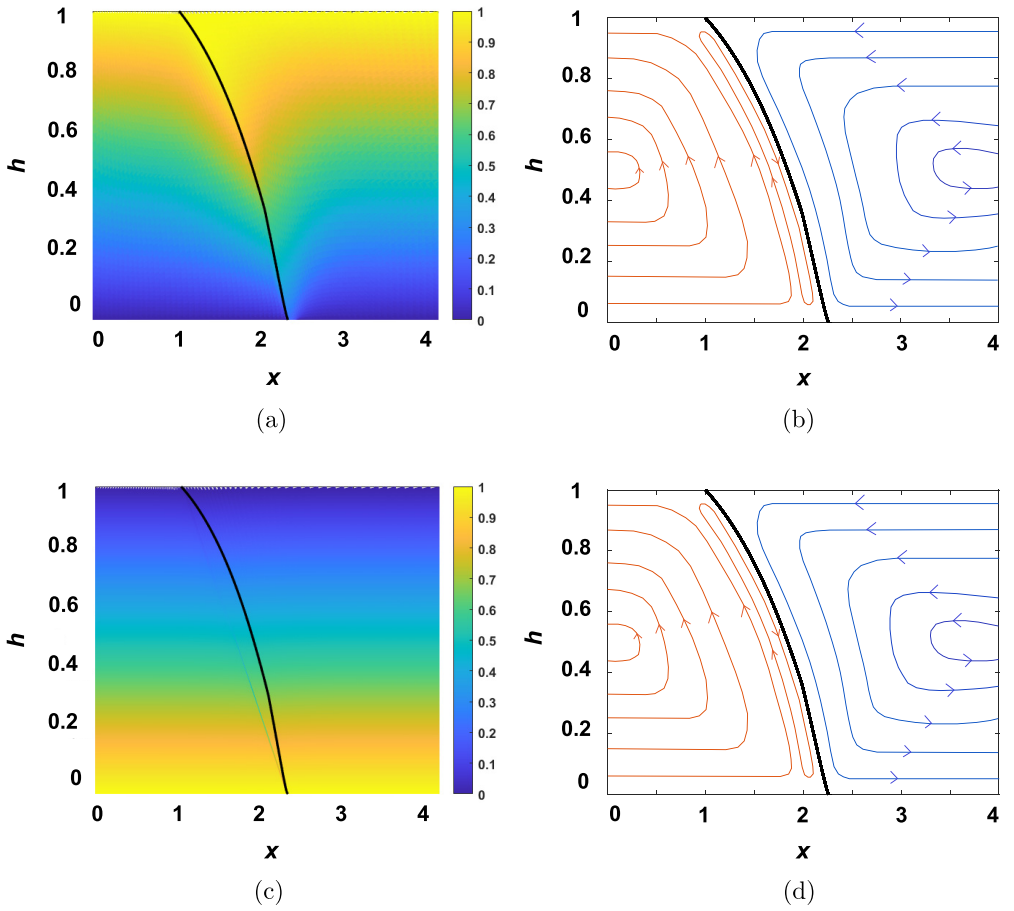

FIG. 3. (a) Temperature contours for the case $M_t > 0$ ($M_t = 1.98$) at Ca $= 4.5$. (b) Streamlines for the case $M_t > 0$ ($M_t = 1.98$) at Ca $= 4.5$. (c) Temperature contours for the case $M_t < 0$ ($M_t = -11.43$) at Ca $= 0.75$. (d) Streamlines for the case $M_t < 0$ ($M_t = -11.43$) at Ca $= 0.75$. The black solid line in all the panels shows the air-liquid interface. In panels (b) and (d), the red lines correspond to air and the blue lines correspond to liquid.

can move horizontally. The maximum interface deformation (indicated by the extent to which the contact line has moved to the right along the bottom plate) occurs for $M_t < 0$, followed by $M_t = 0$ and $M_t > 0$. This indicates that thermal Marangoni flow directed toward the contact line reduces the interface bending at any given Ca, while flow away from the contact line enhances it.

Figure 3 shows the temperature contour plots and streamlines for the cases $M_t > 0$ and $M_t < 0$. For both cases, steady-state solutions near the turning point in the solution families [Fig. 2(a)] are chosen, which represent a system nearing the onset of wetting failure (Ca $\sim$ Ca$_{\text{crit}}$). The interface profile is found to be similar in both cases (see interface shapes shown by the solid black line in the different panels in Fig. 3). This is consistent with the findings discussed in Sec. III A where all the solution families reached Ca$_{\text{crit}}$ at nearly the same θ_M. Indeed,the interface shapes near Ca$_{\text{crit}}$ are nearly the same for all three cases, as illustrated in Fig. 4(a).

In our model, the dimensionless temperature is 0 at the bottom plate and 1 at the top plate for $M_t > 0$, and vice versa for $M_t < 0$. As expected, Fig. 3(a) shows that the temperature decreases as we move from the fixed boundary ($y = 1$) to the substrate ($y = 0$) for $M_t > 0$, and Fig. 3(c) shows that the temperature increases as we move from the fixed boundary to the substrate for $M_t < 0$. For

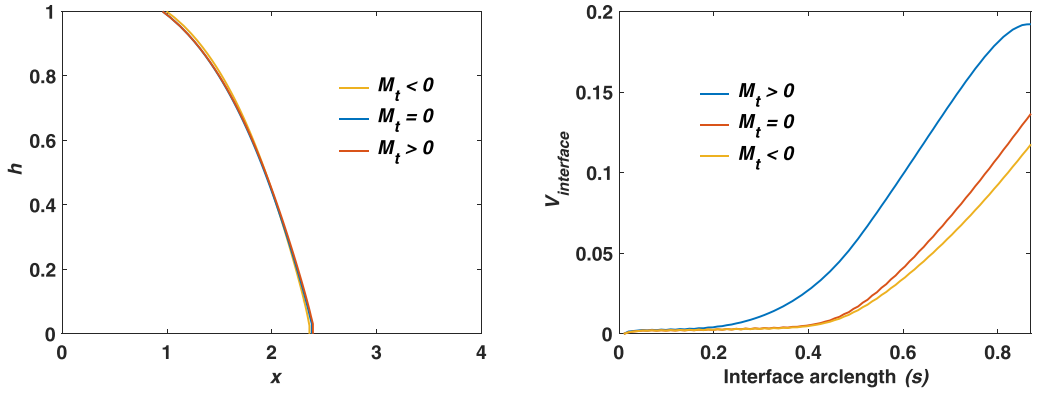

(a) (b)

FIG. 4. (a) Interface profiles for all three cases near their respective $\mathrm{Ca}_{\mathrm{crit}}$: $\mathrm{Ca} = 4.5$ for $M_t > 0$, $\mathrm{Ca} = 1.1$ for $M_t = 0$, and $\mathrm{Ca} = 0.75$ for $M_t < 0$. (b) Variation of the tangential velocity magnitude at the interface with the interface arclength (s) for $\mathrm{Ca} = 0.75$.

$M_t > 0$, there is a variation in the temperature along the horizontal axis as we move closer to the interface, whereas for $M_t < 0$, the temperature does not change as much along the horizontal axis. This result is explained by considering the flow patterns and velocity magnitudes in both phases.

The liquid experiences viscous drag due to the motion of the bottom plate. Consequently, the liquid present near the fixed upper plate is pulled toward the contact line at the bottom plate [13]. As a result, a rolling flow pattern is exhibited in the liquid phase as seen in Figs. 3(b) and 3(d). This is consistent with the findings of Liu *et al.*, where the qualitative features of the flow do not change in the presence of surfactant-induced Marangoni flow for the parallel-plate geometry [11].

For $M_t > 0$, the Marangoni flow generated toward the contact line at the bottom plate supports the rolling flow pattern in the liquid, whereas for $M_t < 0$, flow away from the contact line opposes it. Figure 4(b) shows the variation in the magnitude of the tangential velocity at the air-liquid interface with the interface arclength (s) for $M_t > 0$ and $M_t < 0$, at a fixed Ca. The top contact line is defined as $s = 0$, and the bottom contact line is defined as $s = 1$, so that s increases as we move from the top plate to the bottom plate [Fig. 1(a)]. Results are shown from $s = 0$ to $s = 0.9$, as sharp velocity gradients and the highly dense node distribution near the contact line make it difficult to extract reliable velocity magnitudes near $s = 1$.

As the Marangoni flow for $M_t > 0$ supports the rolling flow motion in the liquid, the magnitude of tangential velocity at the interface is expected to increase as compared to the case with no Marangoni flow ($M_t = 0$). In contrast, the tangential velocity magnitude is expected to decrease for $M_t < 0$, as the Marangoni flow opposes the rolling flow motion. This is consistent with the trend observed in Fig. 4(b), where $M_t > 0$ has the largest velocity magnitude, followed by $M_t = 0$ and $M_t < 0$. For each case, the velocity magnitude increases as we move from the stationary top plate ($s = 0$) to the moving bottom plate ($s = 1$), as expected.

For $M_t > 0$, it turns out that the largest vertical velocity components near the interface are nearly an order of magnitude larger than the vertical velocity components far from the interface. This is a result of the increase in the velocity magnitudes at the interface caused by the downward Marangoni flow [Fig. 4(b)]. In contrast, for $M_t < 0$, the upward Marangoni flow leads to vertical velocity components near the interface that are only about 10–20% larger in magnitude than those in the bulk. For $M_t > 0$, the larger vertical velocity gradients lead to a kink in the temperature contours [Fig. 3(a)], which is not seen for $M_t < 0$ [Fig. 3(c)]. As one moves in the horizontal direction away from the interface, the vertical velocity gradients decrease for $M_t > 0$, so the kink in temperature

contours becomes less pronounced, and this gives rise to the horizontal temperature gradients in Fig. 3(a).

A slender recirculation zone is seen in the air phase for both cases [Figs 3(b) and 3(d)], where the air flows down along the interface and changes its direction near the contact line at the bottom plate. This leads to sharp velocity and stress gradients in the air phase near the contact line which play an important role in the wetting-failure mechanism, as discussed in Sec. IV. The qualitative features of the flow pattern remain the same in the absence of thermal Marangoni flow, and these results are consistent with prior work [13].

Finally, we briefly comment on the incompressibility assumption for the air. Because the air film near the dynamic contact line becomes elongated as the critical capillary number is approached, the air-pressure gradients in the horizontal direction are much greater than those in the vertical direction [13]. Additionally, Fig. 3 indicates that the temperature gradients in the horizontal direction are much less than those in the vertical direction. Assuming ideal-gas behavior, analysis of the temperature fields in Fig. 3 (and the associated pressure fields from the simulations, which assume incompressible flow) reveals that air density would vary by 5% at most over the entire air phase, relative to the isothermal case. Near the dynamic contact line, this variation is much smaller since the air film there is much thinner than the distance between the plates. Together, these observations imply that any air-density changes due to temperature are unlikely to significantly influence the air-pressure gradients in the horizontal direction, which are primarily responsible for driving the air flow [13,34,35]. This suggests that the incompressibility assumption is likely reasonable so that the resulting predictions, which isolate the influence of thermocapillarity, are qualitatively accurate.

IV. WETTING-FAILURE MECHANISM

In the absence of Marangoni flow, wetting failure occurs when the capillary-stress gradients (arising due to the variation in the interface curvature) can no longer support the pressure gradients required to push the air away from the contact line [13]. It was found that the presence of solutal Marangoni flow increases the air-pressure-gradient magnitude near the contact line and causes wetting-failure at a lower critical capillary number [11]. In this section, the influence of thermal Marangoni flow on the wetting-failure mechanism is discussed.

It is useful to estimate how capillary-stress gradients and air-pressure gradients scale near the contact line at the bottom plate as these quantities play a crucial role in the wetting-failure mechanism. Simplifying the governing equations using lubrication theory yields the following scaling for the air-pressure-gradients at the IP [13,22]:

$$\left|\frac{dP}{dx}\right| \sim \frac{\chi}{{h_f}^2}, \tag{4.1}$$

where χ is the viscosity ratio and h_f is the height of the inflection point [see Fig. 1(b)]. On applying the Navier slip condition (2.10), it is found that the interface curvature κ scales as $\ln(r)$ [29]. As a consequence, the capillary-stress gradients at the IP scale as:

$$\frac{1}{\mathrm{Ca}}\left|\frac{d\kappa}{dx}\right| \sim \frac{1}{\mathrm{Ca}}\left(\frac{1}{r_f}\right), \tag{4.2}$$

where Ca is the capillary number and r_f is the distance between the contact line and the IP [Fig. 1(b)]. It should be noted that (4.2) is valid only in the limit $1/h_f \gg \lambda$, where λ is the dimensionless slip length [13].

Figure 5(a) shows the variation of stress-gradient magnitudes (capillary-stress gradient and air-pressure gradient) at the IP with Ca for all the cases. The lines represent the values obtained using the scaling relations (4.1) and (4.2), the circles represent the numerically obtained values of the air-pressure-gradient magnitude, and the diamonds represent the numerically obtained values of the capillary-stress-gradient magnitude. There is reasonably good agreement between numerical

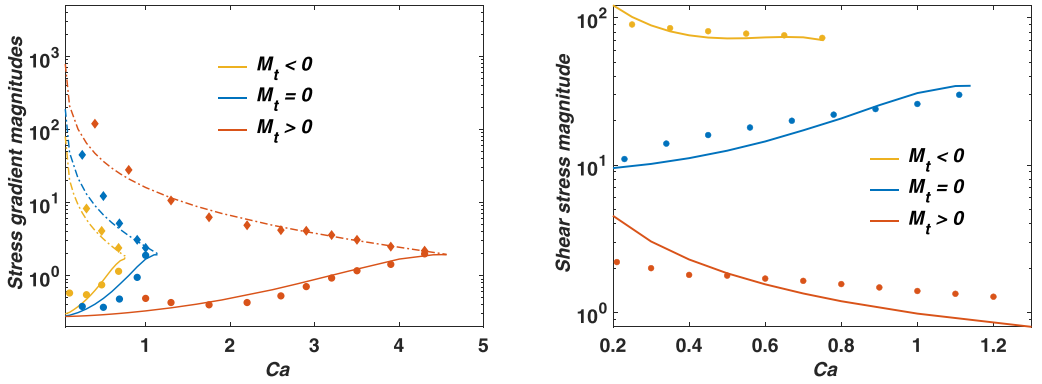

FIG. 5. (a) Stress-gradient magnitude at the IP versus Ca. The solid lines represent the scaling relation (4.1) and the dashed lines represent the scaling relation (4.2). The circles represent air-pressure-gradient magnitudes obtained from numerical simulations and the diamonds represent capillary-stress-gradient magnitudes obtained from numerical simulations. (b) Shear-stress magnitude at IP versus Ca. The red and yellow lines represent the scaling relation (4.4) and the blue line represents the scaling relation (4.3). The circles represent results obtained from numerical simulations.

solutions and the scaling relations for all the cases. The air-pressure gradients have the largest magnitude for $M_t < 0$, followed by $M_t = 0$ and $M_t > 0$. Additionally, the air-pressure gradients rise more steeply as Ca increases for $M_t < 0$. This indicates that thermal Marangoni flow directed away from the contact line ($M_t < 0$) increases the air-pressure-gradient magnitude, making it more difficult to push air away from the contact line, whereas flow toward the contact line ($M_t > 0$) reduces the air-pressure-gradient magnitude.

Marangoni flow directed away from the contact line reduces the capillary-stress-gradient magnitude at any given Ca. The capillary-stress-gradient magnitude depends on the interface curvature gradient [see (4.2)], and this result is attributed to the influence of thermal Marangoni flow on the interface shape (discussed in Sec. III B). Flow away from the contact line causes more interface elongation, which reduces the interface curvature gradient at the IP and consequently reduces the capillary-stress-gradient magnitude. For all the cases, the capillary-stress gradient magnitude matches the air-pressure-gradient magnitude at the respective $\mathrm{Ca}_{\mathrm{crit}}$. This indicates that wetting failure occurs when the capillary-stress gradients near the contact line at the bottom plate can no longer support the air-pressure gradients required to push the air away.

The air-pressure-gradient magnitude at the IP is dependent on the height of the inflection point h_f [see (4.1)], which serves as a reasonable estimate for the air-film thickness [11,22,36,37]. Figure 6(a) shows the variation of h_f with Ca. The lowest h_f is found for $M_t < 0$, followed by $M_t = 0$ and $M_t > 0$. This indicates that Marangoni flow away from the contact line ($M_t < 0$) leads to thinning of the air film, which results in a larger air-pressure-gradient magnitude [Fig. 5(a)]. In contrast, Marangoni flow toward the contact line ($M_t > 0$) thickens the air film and lowers the air-pressure gradients.

The shear-stress magnitude in air ($\mathbf{n} \cdot \mathbf{T} \cdot \mathbf{t}|_{\mathrm{air}}$) at the IP is compared for all the cases to gain insight into the influence of Marangoni stresses on the air-film thickness. On applying lubrication theory, the shear stress in the absence of Marangoni flow scales as:

$$\mu_{\mathrm{air}} \left| \frac{du}{dy} \right| \sim \mu_{\mathrm{air}} \frac{U}{h_f}, \tag{4.3}$$

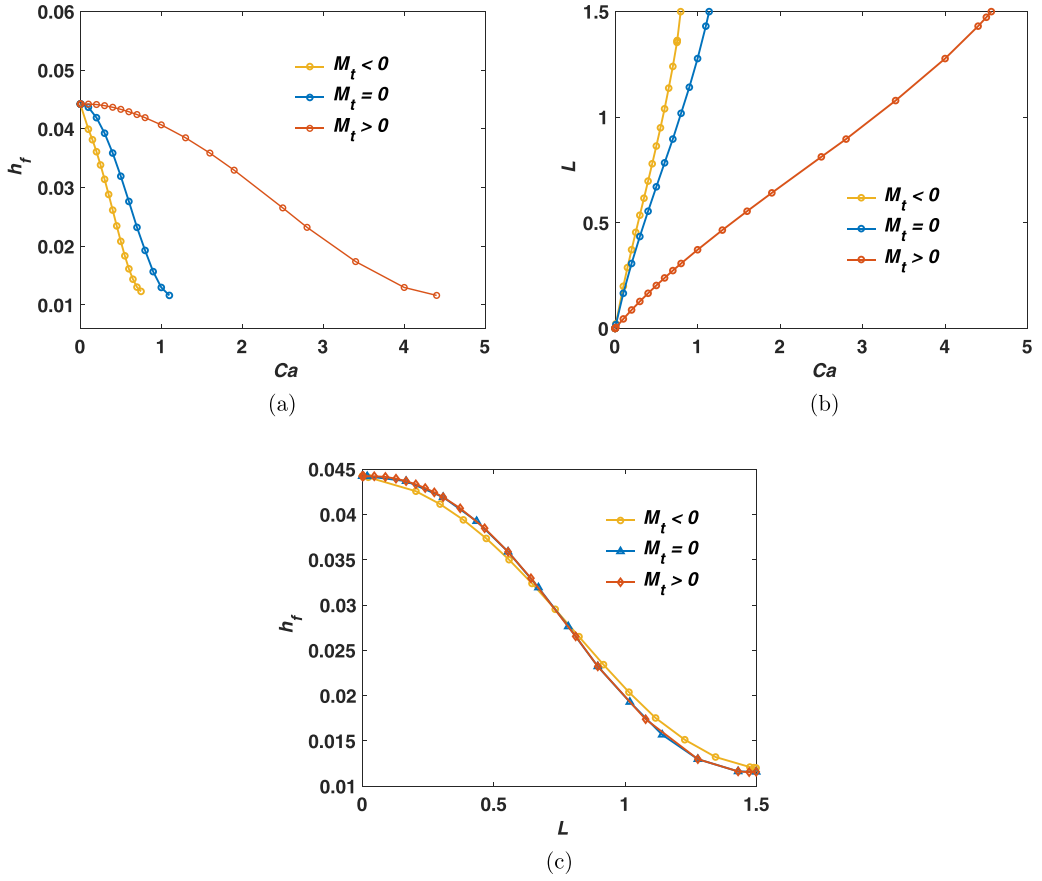

FIG. 6. (a) Inflection point height (h_f) versus Ca. (b) Horizontal length of the interface (L) versus Ca. (c) Inflection point height (h_f) versus horizontal length of the interface (L).

where μ_{air} is the air viscosity and U is the substrate speed. In the presence of Marangoni flow, the shear stress scales as:

$$\mu_{\text{air}} \left| \frac{du}{dy} \right| \sim \frac{\sigma_m}{L}, \tag{4.4}$$

where σ_m is the mean surface tension and L is the horizontal length of the interface [Fig. 1(a)]. The difference in scaling relations is a consequence of the tangential stress balance at the interface (2.6), as the term with the surface-tension gradient becomes zero for $M_t = 0$.

Figure 5(b) shows the shear-stress magnitude in air at the IP for all the cases. The lines represent the values obtained from the scaling relations (4.3) and (4.4), and the circles represent numerically obtained values. Reasonably good agreement is seen between the numerically obtained values and the scaling relations. At any given Ca, the shear-stress magnitude is larger for $M_t < 0$, followed by $M_t = 0$ and $M_t > 0$. This is a consequence of the tangential stress balance (2.6), where $M_t < 0$ increases the shear-stress magnitude in air, and $M_t > 0$ reduces it, as compared to $M_t = 0$. A larger shear-stress magnitude is indicative of a sharp velocity gradient, such that the velocity changes over a shorter distance, leading to a thinner air film for $M_t < 0$. In contrast, a thicker air film is expected due to a lower shear-stress magnitude for $M_t > 0$. The shear-stress magnitude calculations [Fig. 5(b)] are consistent with the air-film thickness calculations [Fig. 6(a)].

Figure 6(b) shows the variation of the horizontal length of the interface (L) with Ca. The interface consistently elongates as the capillary number increases for all the cases. Thus, the shear-stress magnitude in the presence of thermal Marangoni flow ($M_t \neq 0$) is expected to decrease with increasing Ca [see (4.4)], whereas the shear-stress magnitude in the absence of thermal Marangoni flow [which is inversely proportionate to h_f, see (4.3)] is expected to increase with increasing Ca, as h_f decreases with increasing Ca [Fig. 6(a)]. This is consistent with the shear-stress magnitude calculations [Fig. 5(b)]. The interface elongation is larger for $M_t < 0$ at any given Ca, followed by $M_t = 0$ and $M_t > 0$, which is consistent with the interface profiles [Fig. 2(b)].

Figure 6(c) shows the variation of the air-film thickness (h_f) with the interface elongation (L). h_f decreases with increasing L for all the cases, which is consistent with the results illustrated in Figs. 6(a) and 6(b) (h_f decreases with increasing Ca, and L increases with increasing Ca). Moreover, all the curves collapse onto each other, indicating a similarity in the evolution of the interface shape for all the cases.

The above results allow us to draw some conclusions about the mechanism of dynamic wetting failure in the presence of thermal Marangoni stresses. In the absence of Marangoni stresses, the tangential (shear) stresses in the air and liquid must be equal at the interface. For thermal Marangoni flow directed away from the contact line ($M_t < 0$), the tangential stress in the air becomes higher to balance the Marangoni stress at the interface and the tangential stress in the liquid. The higher tangential stress in the air is achieved by the development of a thinner air film. But the thinner air film also causes larger air-pressure gradients, and the resulting interface deformation produces smaller capillary-stress gradients. As a consequence, wetting failure occurs at a lower speed (lower $\mathrm{Ca_{crit}}$). For thermal Marangoni flow directed toward the contact line ($M_t > 0$), the tangential stress in the air becomes lower, which is achieved by the development of a thicker air film. The thicker air film lowers the air-pressure gradients and increases the capillary-stress gradients, thereby postponing wetting failure to higher speeds (higher $\mathrm{Ca_{crit}}$). Thus, the mechanisms of dynamic wetting failure in the presence and absence of Marangoni stresses both involve a balance between air-pressure gradients and capillary-stress gradients, with Marangoni stresses influencing both via the tangential stress balance.

V. CONCLUSIONS

We developed a two-dimensional hydrodynamic model to study the effects of thermal Marangoni flow on dynamic wetting failure in a parallel-plate geometry. It is found that the direction of thermal Marangoni flow influences the value of the critical capillary number at which wetting failure occurs ($\mathrm{Ca_{crit}}$). Compared to a system with no thermal Marangoni flow, thermocapillary flow toward the contact line at the bottom plate delays wetting failure to a higher $\mathrm{Ca_{crit}}$, while thermocapillary flow away from the contact line causes wetting failure at a lower $\mathrm{Ca_{crit}}$. Wetting failure occurs when the capillary-stress gradients cannot match the air-pressure-gradients near the contact line, and thermal Marangoni flow influences the mechanism by changing the magnitudes of these gradients.

Marangoni flow away from the contact line leads to more interface bending and elongation, resulting in the formation of a thinner air film near the contact line. The thinning of the air film can be explained by a large shear-stress magnitude in the air phase, which indicates the presence of steep velocity gradients, and a shorter distance over which the velocity changes. A thinner air film leads to larger air-pressure-gradient magnitudes, which cannot be balanced by the capillary-stress gradients, causing the entrainment of air into the liquid and consequently wetting failure at a lower $\mathrm{Ca_{crit}}$. In contrast, Marangoni flow toward the contact line reduces the interface elongation and forms a thicker air film. This decreases the air-pressure-gradient magnitude and allows the air to be pushed away from the contact line at a higher $\mathrm{Ca_{crit}}$.

Above the critical capillary number, the flow is expected to become three-dimensional and unsteady [5]. This is beyond the regime of the present simulations, which are for steady two-dimensional flows. Recent work has revealed rather rich dynamics in two-dimensional time-dependent flows [38]; the influence of thermocapillarity on these dynamics remains an open issue.

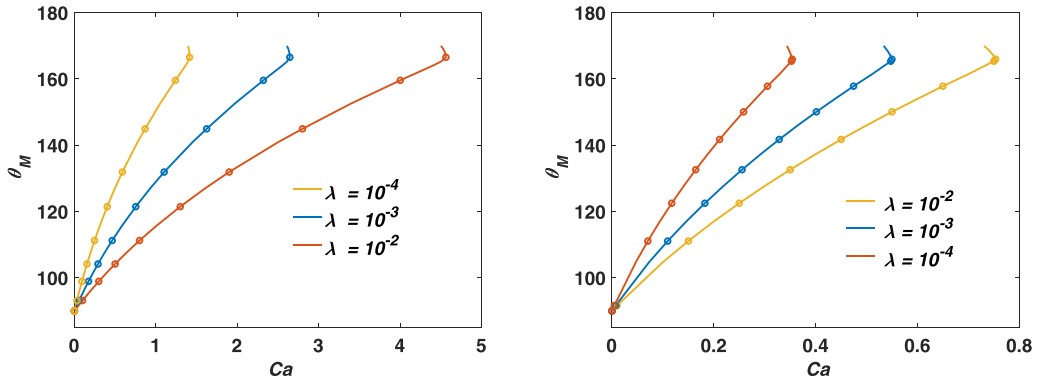

FIG. 7. (a) Solution families for $M_t > 0$ when (i) $\lambda = 10^{-4}$ (yellow curve, $7.58 < M_t < 9936.2$), (ii) $\lambda = 10^{-3}$ (blue curve, $4.31 < M_t < 9901.7$), and (iii) $\lambda = 10^{-2}$ (red curve, $1.28 < M_t < 9893.4$). (b) Solution families for $M_t < 0$ when (i) $\lambda = 10^{-4}$ (red curve, $-9914.6 < M_t < -8.32$), (ii) $\lambda = 10^{-3}$ (blue curve, $-9883.1 < M_t < -7.19$), and (iii) $\lambda = 10^{-2}$ (yellow curve, $-9821.7 < M_t < -5.76$).

As discussed in Sec. III A, model calculations show that modest temperature differences can lead to significant changes in the critical substrate speed at which wetting failure occurs, suggesting a novel strategy for designing faster coating processes through the application of thermal Marangoni flow. For example, in a slot-die coating process, the slot-die could be heated so that the coating liquid has a higher temperature near the slot-die than it has near the substrate. The potential for this strategy to delay wetting failure provides a compelling motivation for complementary experiments, and for more detailed modeling that accounts for the temperature dependence of material properties.

ACKNOWLEDGMENTS

This material is based on work supported by the National Science Foundation under Grant No. CBET-1935968. We thank V. Charitatos, C. Parrish, and S. Pawar for helpful discussions.

APPENDIX

1. Influence of the dimensionless slip length

In the absence of thermal Marangoni flow, it is found that $\mathrm{Ca}_{\mathrm{crit}}$ increases with dimensionless slip length. [5,13,22]. Figure 7 shows that $\mathrm{Ca}_{\mathrm{crit}}$ increases with λ for both $M_t > 0$ and $M_t < 0$, consistent with this prior work.

2. Influence of temperature gradient

Temperature differences of $\Delta T = T_t - T_b = 5^{\circ}\mathrm{C}$, and $\Delta T = T_t - T_b = -5^{\circ}\mathrm{C}$ are used to perform the calculations presented in Sec. III. Figure 8 shows solution families for different vales of ΔT. For $M_t > 0$, $\mathrm{Ca}_{\mathrm{crit}}$ increases with the temperature difference. A larger temperature difference corresponds to a stronger thermal Marangoni flow toward the contact line, which reduces the extent of interface bending and delays wetting failure to higher $\mathrm{Ca}_{\mathrm{crit}}$. For $M_t < 0$, a more negative temperature difference increases the Marangoni flow away from the contact line, which increases interface bending and causes wetting failure at lower $\mathrm{Ca}_{\mathrm{crit}}$.

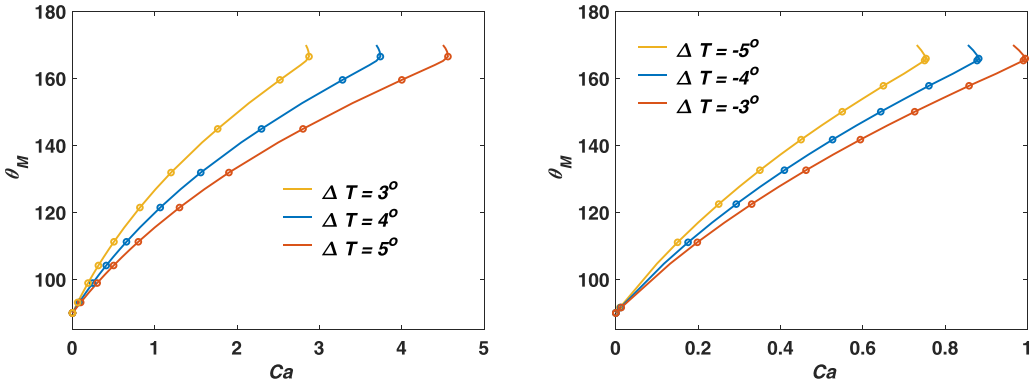

FIG. 8. (a) Solution families for different values of $\Delta T = T_t - T_b$: (i) 3°C (yellow curve, $0.86 < M_t < 5973.6$), (ii) 4°C (blue curve, $1.13 < M_t < 7428.2$), and (iii) 5°C (red curve, $1.28 < M_t < 9893.4$), where T_t is the temperature of the top plate, and T_b is the temperature of the bottom plate. (b) Solution families for $\Delta T = T_t - T_b$: (i) −5°C (yellow curve, $-9821.7 < M_t < -5.76$), (ii) −4°C (blue curve, $-8714.3 < M_t < -3.13$), and (iii) −3°C (red curve, $-6932.9 < M_t < -1.65$).

[1] H. A. Stone, A. D. Stroock, and A. Ajdari, Engineering flows in small devices: Microfluidics toward a lab-on-a-chip, Annu. Rev. Fluid Mech. **36**, 381 (2004).

[2] J. C. Baret, Surfactants in droplet-based microfluidics, Lab Chip **12**, 422 (2012).

[3] C. E. Brown and E. L. Neustadter, The wettability of oil/water/silica systems with reference to oil recovery, J. Can. Petrol. Technol. **19**, 100 (1980).

[4] G. Lu, X. Wang, and Y. Duan, A critical review of dynamic wetting by complex fluids: From newtonian fluids to non-newtonian fluids and nanofluids, Adv. Colloid Interface Sci. **236**, 43 (2016).

[5] E. Vandre, M. S. Carvalho, and S. Kumar, Characteristics of air entrainment during dynamic wetting failure along a planar substrate, J. Fluid Mech. **747**, 119 (2014).

[6] T. D. Blake and K. J. Ruschak, *Wetting: Static and Dynamic Contact Lines* (Springer Netherlands, Dordrecht, 1997), pp. 63–97.

[7] S. J. Weinstein and K. J. Ruschak, Coating flows, Annu. Rev. Fluid Mech. **36**, 29 (2004).

[8] C. V. Sternling and L. E. Scriven, Interfacial turbulence: Hydrodynamic instability and the marangoni effect, AIChE J. **5**, 514 (1959).

[9] J. C. Berg, *Introduction to Interfaces and Colloids: The Bridge to Nanoscience* (World Scientific, Singapore, 2009).

[10] R. Tadmor, Marangoni flow revisited, J. Colloid Interface Sci. **332**, 451 (2009).

[11] C.-Y. Liu, E. Vandre, M. S. Carvalho, and S. Kumar, Dynamic wetting failure in surfactant solutions, J. Fluid Mech. **789**, 285 (2016).

[12] C.-Y. Liu, M. S. Carvalho, and S. Kumar, Mechanisms of dynamic wetting failure in the presence of soluble surfactants, J. Fluid Mech. **825**, 677 (2017).

[13] E. Vandre, M. S. Carvalho, and S. Kumar, On the mechanism of wetting failure during fluid displacement along a moving substrate, Phys. Fluids **25**, 102103 (2013).

[14] C.-Y. Liu, E. Vandre, M. S. Carvalho, and S. Kumar, Dynamic wetting failure and hydrodynamic assist in curtain coating, J. Fluid Mech. **808**, 290 (2016).

[15] C.-Y. Liu, M. S. Carvalho, and S. Kumar, Dynamic wetting failure in curtain coating: Comparison of model predictions and experimental observations, Chem. Eng. Sci. **195**, 74 (2019).

[16] D. Kang, A. Nadim, and M. Chugunova, Marangoni effects on a thin liquid film coating a sphere with axial or radial thermal gradients, Phys. Fluids **29**, 072106 (2017).

[17] C. Li, D. Zhao, J. Wen, and X. Lu, Numerical investigation of wafer drying induced by the thermal Marangoni effect, Int. J. Heat Mass Transf. **132**, 689 (2019).
[18] K. Zakaria, M. A. Sirwah, and S. A. Alkharashi, A two-layer model for superposed electrified Maxwell fluids in presence of heat transfer, Commun. Theor. Phys. **55**, 1077 (2011).
[19] X. Ding, J. Liu, and T. A. L. Harris, A review of the operating limits in slot die coating processes, AIChE J. **62**, 2508 (2016).
[20] C. Huh and L. E. Scriven, Hydrodynamic model of steady movement of a solid/liquid/fluid contact line, J. Colloid Interface Sci. **35**, 85 (1971).
[21] T. S. Chan, S. Srivastava, A. Marchand, B. Andreotti, L. Biferale, F. Toschi, and J. H. Snoeijer, Hydrodynamics of air entrainment by moving contact lines, Phys. Fluids **25**, 074105 (2013).
[22] E. Vandre, M. S. Carvalho, and S. Kumar, Delaying the onset of dynamic wetting failure through meniscus confinement, J. Fluid Mech. **707**, 496 (2012).
[23] V. Charitatos, W. J. Suszynski, M. S. Carvalho, and S. Kumar, Dynamic wetting failure in shear-thinning and shear-thickening liquids, J. Fluid Mech. **892**, A1 (2020).
[24] P. R. Schunk, P. A. Sackinger, and R. R. Rao, *Goma—A Full-Newton Finite Element Program for Free and Moving Boundary Problems with Coupled Fluid/Solid Momentum, Energy, Mass, and Chemical Species Transport: User's Guide*, Vol. 1 (Sandia National Laboratories, Albuquerque, 1996).
[25] Coreform LLC, Coreform Cubit. Version 2020.2, http://coreform.com.
[26] D. W. Green and M. Z. Southard, *Perry's Chemical Engineers' Handbook, 9th Edition* (McGraw-Hill Education, New York, 2018).
[27] T. D. Blake, The physics of moving wetting lines, J. Colloid Interface Sci. **299**, 1 (2006).
[28] M. C. T. Wilson, J. L. Summers, Y. D. Shikhmurzaev, A. Clarke, and T. D. Blake, Nonlocal hydrodynamic influence on the dynamic contact angle: Slip models versus experiment, Phys. Rev. E **73**, 041606 (2006).
[29] J. H. Snoeijer and B. Andreotti, Moving contact lines: Scales, regimes, and dynamical transitions, Annu. Rev. Fluid Mech. **45**, 269 (2013).
[30] J. Eggers, Existence of receding and advancing contact lines, Phys. Fluids **17**, 082106 (2005).
[31] R. Ledesma-Aguilar, A. Hernández-Machado, and I. Pagonabarraga, Theory of Wetting-Induced Fluid Entrainment by Advancing Contact Lines on Dry Surfaces, Phys. Rev. Lett. **110**, 264502 (2013).
[32] D. Jacqmin, Onset of wetting failure in liquid–liquid systems, J. Fluid Mech. **517**, 209 (1999).
[33] M. Sbragaglia, K. Sugiyama, and L. Biferale, Wetting failure and contact line dynamics in a Couette flow, J. Fluid Mech. **614**, 471 (2008).
[34] B. J. Bayly, C. D. Levermore, and T. Passot, Density variations in weakly compressible flows, Phys. Fluids **4**, 945 (1992).
[35] J. E. Sprittles, Air entrainment in dynamic wetting: Knudsen effects and the influence of ambient air pressure, J. Fluid Mech. **769**, 444 (2015).
[36] R. L. Hoffman, A study of the advancing interface. I. Interface shape in liquid—gas systems, J. Colloid Interface Sci. **50**, 228 (1975).
[37] R. Burley and R. P. S. Jolly, Entrainment of air into liquids by a high speed continuous solid surface, Chem. Eng. Sci. **39**, 1357 (1984).
[38] J. S. Keeler, D. A. Lockerby, S. Kumar, and J. E. Sprittles, Stability and bifurcation of dynamic contact lines in two dimensions, J. Fluid Mech. **945**, A34 (2022).